

Synchrotron characterization of deep depletion epitaxial GaAs detectors

Alan Owens, M. Bavdaz, S. Kraft, A. Peacock, R. Strade
Space Science Department of ESA, ESTEC, 2200AG Noordwijk, Netherlands

S. Nenonen, H. Andersson, M.A. Gagliardi, T. Gagliardi
Metorex International Oy, P.O. Box 85, FIN-02201 Espoo, Finland

H. Graafsma,
Experimental Division, ESRF, BP220 Avenue des Martyrs, 38043 Grenoble, Cedex France

We report the results of a series of synchrotron characterizations of two epitaxial GaAs detectors of active areas 2.22 mm^2 and thicknesses 40 and 400 microns. In spite of an order of magnitude difference in depletion depths, the detectors were found to have comparable performances at $\sim -40^\circ\text{C}$, with energy resolutions of $\sim 1 \text{ keV}$ fwhm at 7 keV rising to $\sim 2 \text{ keV}$ fwhm at 200 keV and noise floors in the range 1-1.5 keV. At the lower energies, the energy resolution was dominated by leakage current and electromagnetic pick-up. At the highest energies, however, the measured resolutions appear to approach the expected Fano limit; e.g., $\sim 950 \text{ eV}$ at 200 keV. Both detectors were remarkably linear, with average rms non-linearities of 0.2% over the energy range 10-60 keV. By raster scanning the active areas with $20 \times 20 \text{ micron}^2$ monoenergetic photon beams, it was found that the non-uniformity in the spatial response of both detectors was less than 1% and independent of energy. The material used to fabricate the detector is extremely pure. For example, low temperature photoluminescence measurements indicate that the density of the As anti-site defect (EL2) is of the order of 10^{12} cm^{-3} , which is ~ 2 -3 orders of magnitude lower than that generally reported. This indirect measurement of material purity is confirmed by Monte-Carlo simulations of the detector X-ray response, which show that in order to reproduce the observed energy-loss spectra, electron and hole trapping cross-section/density products must be $\ll 1 \text{ cm}^{-1}$.

PACS: 07.85.F, 29.4.W

1. Introduction

In recent years, considerable effort has been expended in producing semiconductor based X-ray detectors with high spectral and high spatial resolution. In practical terms, this means producing pixelated detectors, comprising over 10^3 pixels each less than 100 microns in size, with spectral resolving powers, $E/\Delta E > 20$ at 10 keV. While progress at soft X-rays wavelengths has been spectacular, largely due to the introduction of X-ray sensitive CCD's, progress at higher energies has been slow.

This is because traditional high resolution detectors either suffer from poor detection efficiencies above 10 keV, as in the case of Si based technology, or are very constrained by cryogenic and fabrication problems in the case of Ge based detectors. Recent developments in wide band-gap compound semiconductors have shown that such materials may bridge Ge and Si technologies. In these devices, the band-gap is sufficiently high so they do not require cryogenic cooling but low enough that sub-keV spectral resolution may be achieved at hard X-ray energies. In addition, materials drawn from group III and V compounds have high enough atomic numbers to ensure high detection efficiencies above 10 keV. While the performances of such devices are not yet close to Fano limit (and ultimately, as a result of their higher bandgap, they can never achieve the spectral performances of Si or Ge), spectroscopically they can already satisfy the requirements of most of the anticipated future X-ray astronomy missions above 10 keV. The Space Science Department of ESA has, for a number of years, worked to develop large area compound semiconductor arrays for the next generation of X-ray astrophysics missions. These will ultimately operate in the 1-200 keV energy range with near Fano limited energy resolution. In a previous paper [1] we summarized the results of a series of characterizations of a 1.5 mm diameter, 40 micron thick epitaxial GaAs detector using radioactive sources under full-beam illumination. In this paper, we report on a major extension of that work - the synchrotron characterization of two high purity epitaxial GaAs detectors - the original 40 micron detector and a new 400 micron deep depletion detector. Both devices are identical, being fabricated from the same wafer stock and differ only in the thickness of the epitaxial layer. The new detector was made ten times thicker to try and isolate the electronic and material dependent properties of the X-ray response.

2. Device fabrication

2.1 Material

The detectors were fabricated on semi-insulating GaAs wafers using chemical vapor phase deposition (CVPD) techniques. During material processing and growth, the epi-layers and associated structures were subjected to a variety of analytical tests to characterize the material and the technique of producing ultra-pure GaAs layers. For example, Hall effect measurements show that for the samples used to produce the detectors, the impurity concentrations are $<10^{13} \text{ cm}^{-3}$ and the electron mobilities at 77 K are $2 \times 10^6 \text{ cm}^2\text{V}^{-1}\text{s}^{-1}$. These agree well with cyclotron resonance measurements of non-equilibrium electrons in n_0 -GaAs layers, which show that the mobilities at 1.8 K are $3 \times 10^6 \text{ cm}^2\text{V}^{-1}\text{s}^{-1}$ and the shallow impurity concentration does not exceed $5 \times 10^{12} \text{ cm}^{-3}$. Based on low temperature Photo-luminescence (PL), the density of the As anti-site defect (EL2) is estimated to be of the order of 10^{12} cm^{-3} and the room temperature carrier lifetimes of the order of 1 μs . The corresponding density of EL2

traps in the substrate material is estimated to be about $3 \times 10^{15} \text{ cm}^{-3}$ (which is about one tenth of the values normally obtained for semi-insulating bulk material) and the total impurity concentration $\sim 10^{18} \text{ cm}^{-3}$. Monte-Carlo modeling supports these values (see section 3.4).

2.2 Detectors

Figure 1 shows a cross-sectional view of the detectors. Their characteristics are listed in Table 1. They are 1.5 mm in diameter (physical area = 1.77 mm^2) and consist of a 40 or 400 μm thick epitaxial layer grown onto a 100 μm thick n+ GaAs substrate. A pin structure is then formed by depositing a 5 μm thick p+ layer directly onto the epitaxial layer and then depositing a full ohmic contact (Ni/Au/Ge/Au) on the n+ side. The p+ side is patterned by etching to define the detector (mesa) and guard ring structure, which is intended to reduce surface leakage currents. The guard ring was

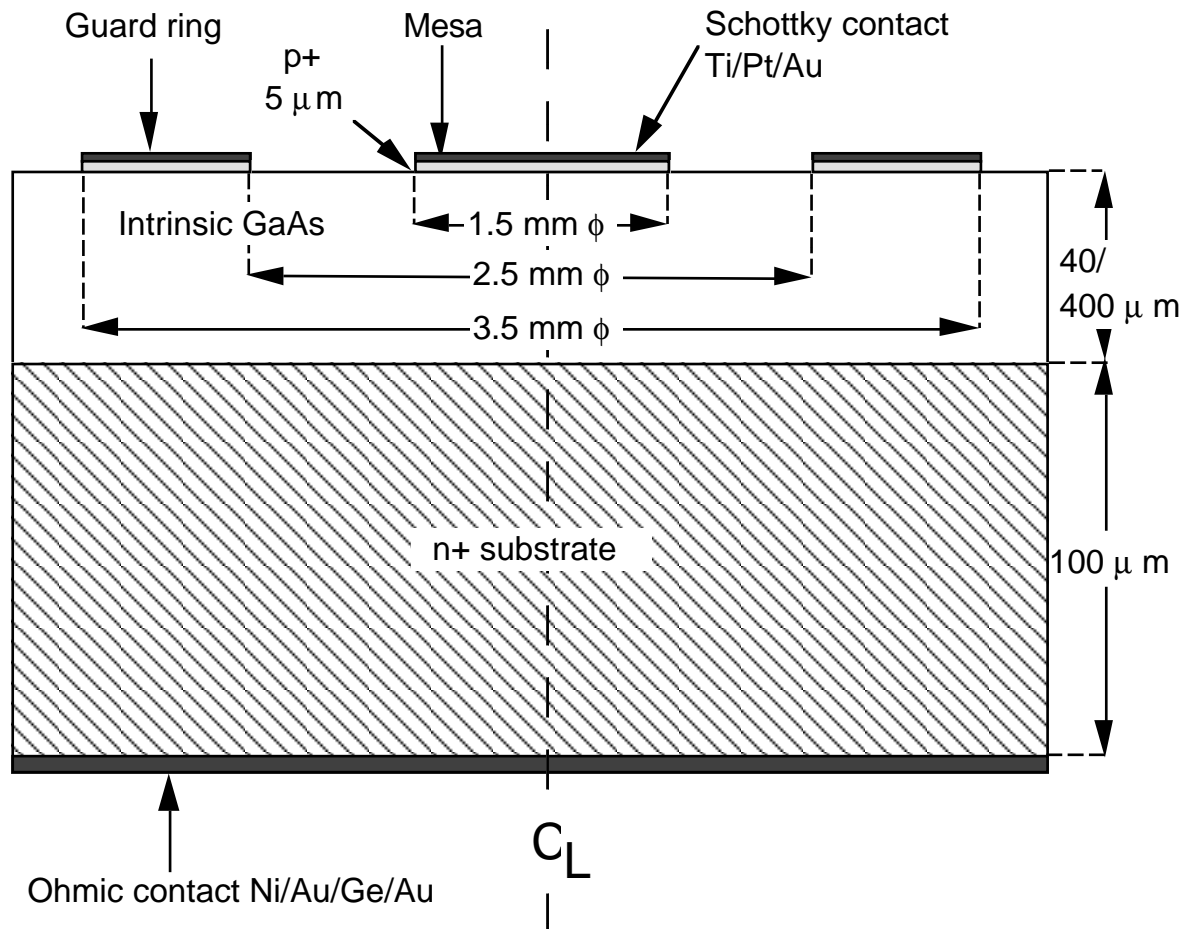


Figure 1. Schematic cross-section of a detector.

not used in the measurements described here. Both the mesa and the guard ring are metalised with alternate depositions of Au/Pt/Ti to form a Schottky contact. The devices are operated as reverse biased diodes with the p+ contact at negative potential.

At the nominal bias, the detector is found to be fully depleted with a very sharp boundary at the conductive n+ GaAs substrate. This has been verified by comparing experimental results with simulation. From the I/V characteristics, the typical current densities at -100V were $<0.04\text{nA/mm}^2$ at room temperature, which is about a factor of 3-100 lower than normally obtained with CVPD detectors and a factor of 10^3 - 10^4 lower than bulk detectors. At nominal biases of -40 V for the 40 μm device and -300 V for the 400 μm device, the leakage currents were 40pA and 100 pA, respectively at room temperature. It is believed that the relatively large value of the leakage current in the 400 micron device, is due to low surface resistivity caused by the repeated etching of the p+ layer. This was necessary, due to a production error in which the p+ layer was allowed to grow to a thickness much greater than the nominal 5 μm . It was eventually etched back to a thickness of $\sim 25\mu\text{m}$.

Table 1. Device Characteristics. The performance figures quoted are for HASYLAB measurements.

Parameter	40 micron device	400 micron device
Diameter (physical)	1.5 mm	1.5 mm
Active area	2.22 mm ²	2.22 mm ²
Depletion depth	40 μm	400 μm
Dead layer thickness	5 μm	25 μm
Maximum operating bias	-10V (T=17°C) to -80V (T= -40°C)	-150V (T=33°C) to -400V (T= -45°C)
Nominal Bias & operating temp	-40V, -40°C	-300V, -45°C
RT Leakage current @ nominal bias	40 pA	100 pA
FWHM Energy resolution @ 5.9 keV, 20 keV, 60.0 keV	728 eV, 740 eV, 1.1keV @ -39°C	1.1 keV, 1.2 keV, 1.3 keV @ -45°C
Detection efficiency @ 6.4 keV, 20 keV, 60.0 keV	61%, 52%, 4.5%	61%, 86%, 33%

The detectors are mounted on two stage Peltier coolers which are capable of cooling the devices to $\sim -30^\circ\text{C}$. Coupling the hot side of the Peltier to a water cooler allows the detectors to be cooled by an addition -10°C . For the bulk of the measurements described here, the detector temperature was set to $\sim -40^\circ\text{C}$ for the 40 micron device and -45°C for the 400 micron device. The signal from each detector is extracted from the n+ side by a modified Princeton Gamma Tech PGT P014TR-N preamplifier whose front end FET is also maintained at the detector temperature. The rest of the analog chain consists of an Ortec 671 spectroscopy amplifier that shapes and amplifies the signal prior to digitization. Both the signal amplitude and rise time are digitized by a pair of Canberra 8701 ADCs and processed and stored by a PC.

3. Experimental

X-ray experiments were carried out on the open bending magnet (BM5) high energy beam line at the European Synchrotron Research Facility (ESRF) and the X1 beamline at the Hamburg Synchrotron Laboratory (HASYLAB). Both beamlines use double crystal monochromators to produce highly monochromatic X-ray beams. The energy range covered at the ESRF was 7-35 keV using a Si[111] reflection and at HASYLAB, 6-60 keV (X1) using both Si[311] and Si[511] reflections. The intrinsic energy resolution was typically ~ 1 eV at 10 keV rising to 20 eV at 35 keV. For Si[111] reflections, it was possible to extend some measurements up to ~ 200 keV by using absorbers to amplify higher orders. For the majority of measurements described here, the beam was normally incident on the center at the detectors and had a typical spot size of 20×20 microns².

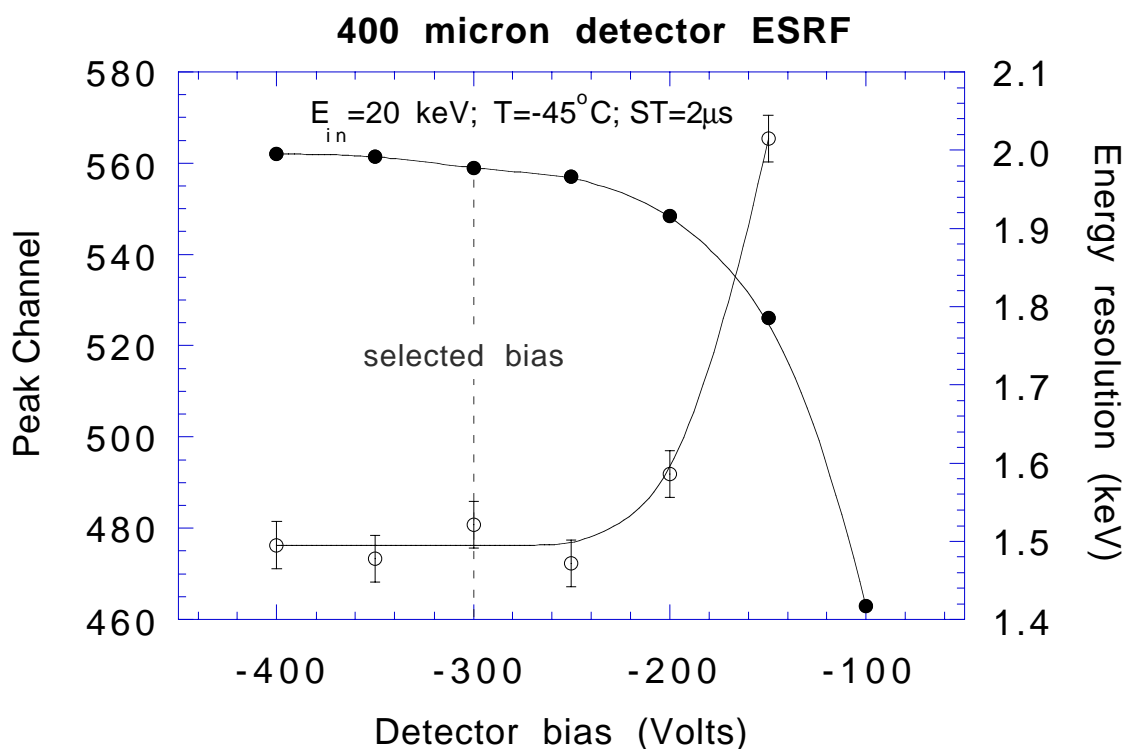


Figure 2. The variation in peak channel (solid data points) and fwhm energy resolution (open data points) for the 400 micron device measured at an incident energy of 20 keV at the ESRF. The curves for the 40 μ m detector look similar, differing only in normalization.

3.1. Device characterization

Figure 2 shows the variation of the peak channel (a) and fwhm (b) as a function of bias for the 400 micron detector measured at an incident energy of 20 keV at the ESRF. For both detectors we see a small variation in the peak channel with bias, being less than 20% for all biases above which the detectors are spectroscopic. Likewise,

above a certain bias (-250V for the 400 micron device and -40V for the 40 micron device) there is little variation (i.e., < 6%) in the fwhm energy resolution.

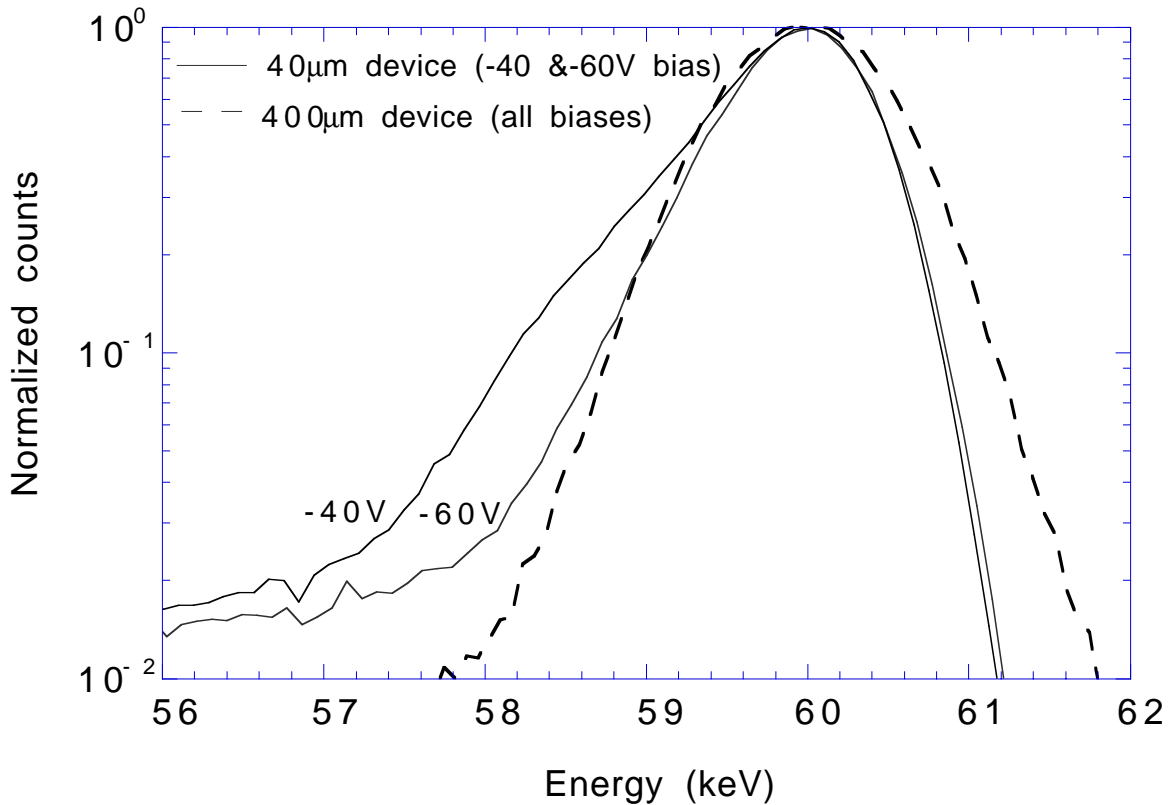


Figure 3. The shape of the peak measured at 60 keV in the 40 micron detector at two biases at HASYLAB. For comparison we also display the shape of the energy loss peak in the 400 micron detector which was found to be very nearly gaussian in shape and independent of bias and energy.

Since the fwhm energy resolution essentially describes the level of noise in the system we have used this parameter as a figure of merit and adjusted the detectors operating conditions to minimize the fwhm. Although the shape of the noise curves (i.e., energy resolution versus shaping time) at each facility were similar, the noise at the ESRF was about 300 eV greater than that measured at HASYLAB - presumably due to electromagnetic interference. However, the values of shaping time and bias which gave the lowest fwhm were the same at each facility, namely 2 μ s and -300 V for the 400 micron detector and 3 μ s and -40 V for the 40 micron device. For the 40 micron detector, the shape of the photopeak was found to be gaussian at X-ray energies <20 keV. Above this energy, the peak shape became increasingly skewed. Increasing the bias to -60 V resulted in a much more symmetric peak shape that appeared tailed rather than skewed. This is illustrated in Figure 3 in which we show both profiles at two biases at an incident X-ray energy of 60 keV. For comparison we also show the 400 micron device peak shape at the same energy and at its nominal bias. Its peak shape was found to be independent of both energy and bias and

therefore all measurements were carried out at a nominal bias of -300 V. For the HASYLAB runs, the 40 micron device was operated at a bias of -60V.

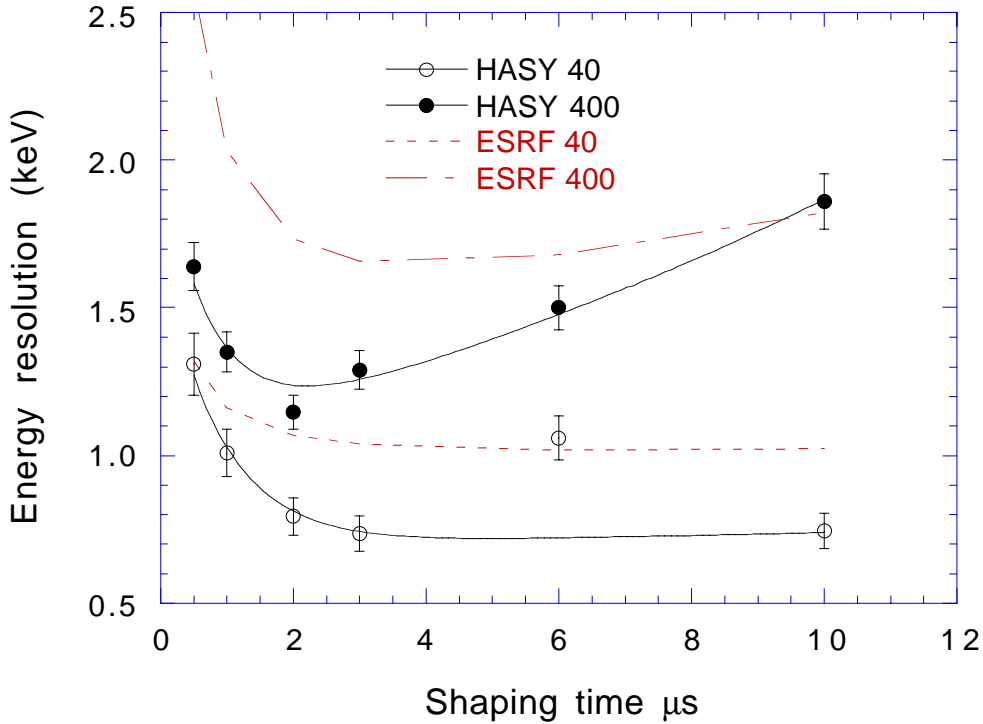


Figure 4. The measured energy resolution of both detectors as a function of shaping time. The incident photon energy was 20 keV. For clarity, we only show data points for HASYLAB data and best-fits to the ESRF data (assuming power law models). The statistical precision of both data sets is similar.

In Figure 4 we show the measured fwhm energy resolutions as a function of amplifier shaping time for both devices measured at HASYLAB and the ESRF at an incident energy of 20 keV. We note that the shape of each detectors noise curve is similar, irrespective of facility. From Figure 4, we see that the noise curves of both detectors display the characteristic $\sim t^{-0.5}$ fall-off expected from series noise at small shaping times. This component results primarily from thermal voltage fluctuations at the gate of the FET and Johnson noise from the equivalent resistance associated with the FET transconductance and bias resistors. At longer shaping times, the response rises quite slowly and is somewhat flatter than the expected $t^{+0.5}$ dependence of the parallel noise arising from shot noise of the leakage current. Since the leakage currents in GaAs are large and their capacitance's low, parallel noise dominates the detector noise response.

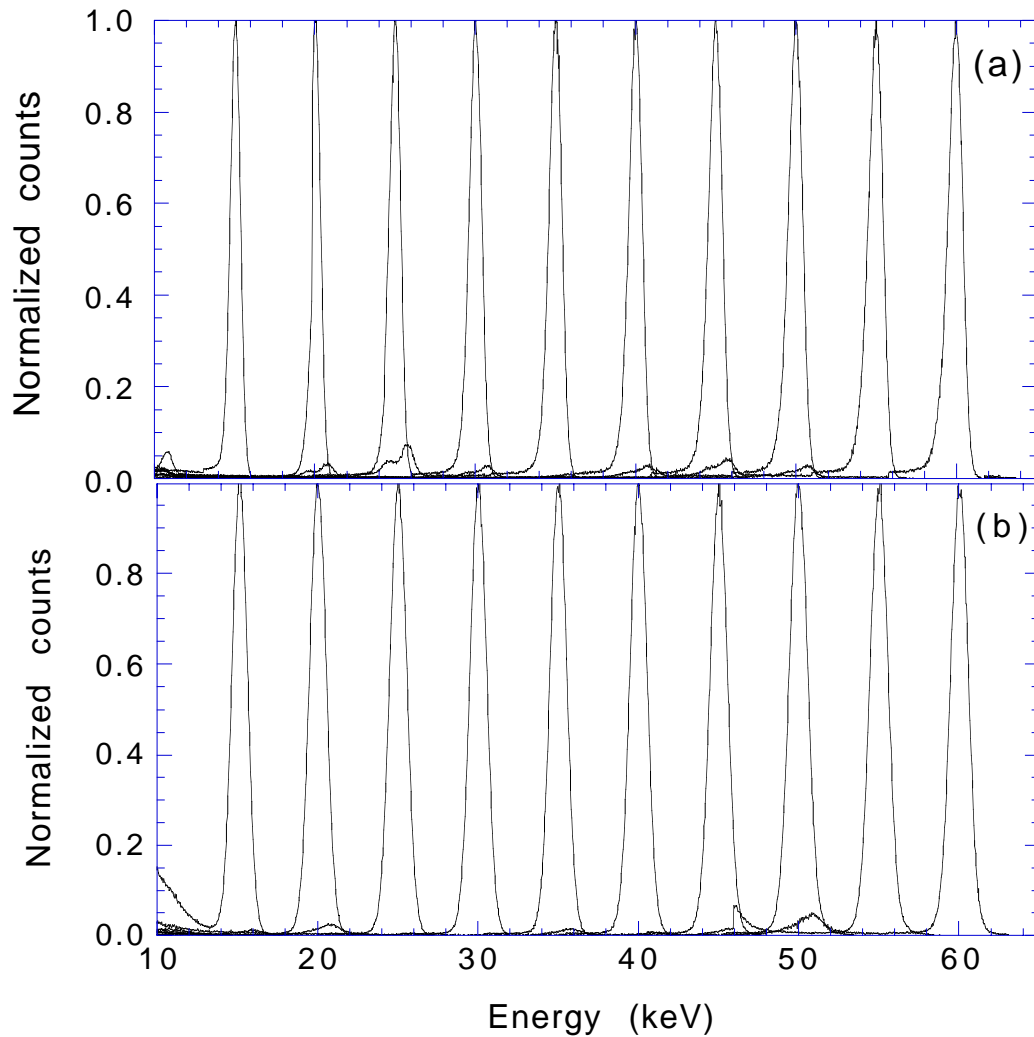


Figure 5. Composite pulse height spectra taken at HASYLAB with the (a) 40 μm and (b) 400 μm detector.

3.2 Linearity

In Figures 5(a) and 5(b) we show a composite of the energy spectra recorded by the 40 and 400 micron detectors in response to monoenergetic radiation at a range of energies from 15 keV to 60 keV. The smaller peaks which appear at an energy of ~ 11 keV below the photopeaks are due to Ga and As fluorescence peaks. Note, that due to its somewhat better energy resolution, these are just resolved in the 40 micron device. The noise threshold (defined to be the lowest energy where low energy noise attains an amplitude of 0.5 of the photopeak) was 0.7 keV and 1.2 keV for the 40 micron and 400 micron devices, respectively. The response of both detectors is remarkably linear with the regression coefficients for the best-fit peak channel number versus incident X-ray energies generally in excess of 99.99 for the energy range 10 to 60 keV. In figure 6, we show the linearity curve for the 400 μm device measured at the ESRF over the

extended energy range 7 to 175 keV. In this case, the average rms non-linearity is worse at 0.8%, but this is probably largely due to the inherent non-linearity in the monochromator when operated over such a large energy range. Only in the vicinity of the Ga and As K-absorption edges can significant deviations be seen which may be attributed to the abrupt change in absorption depth across the edges. This results in a slight change in peak shape, which under a gaussian approximation, results in an error in determining the centroid of the peak. From the graph of the residuals, we see that this error is small, amounting to a peak shift of only $\sim 2\%$ of the expected peak value. However, ignoring data taken around the Ga and As edges the average non-linearity on data points for both detectors is typically $\sim 0.2\%$ rms over the energy range 10-60 keV.

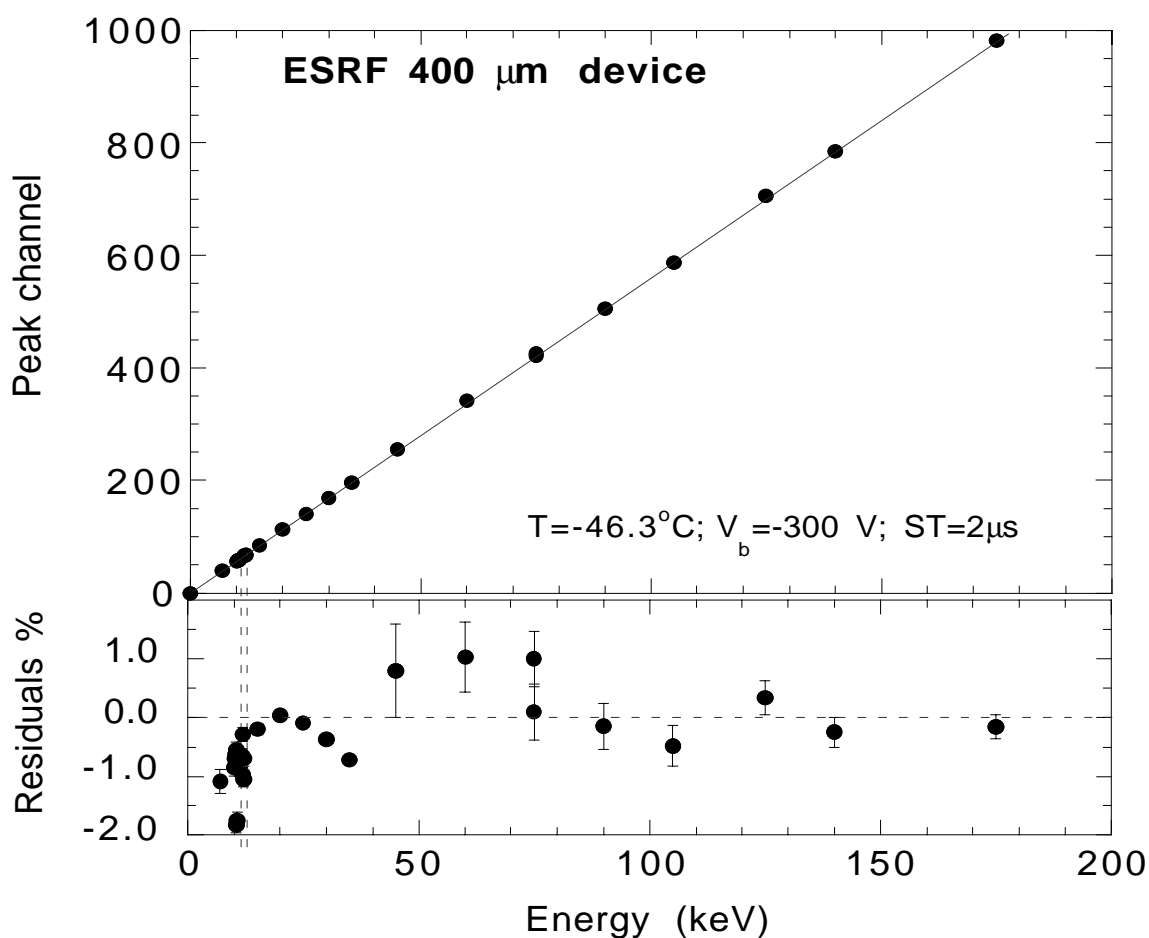


Figure 6. The linearity of the 400 micron device measured at the ESRF over the energy range 7 keV to 175 keV. The lower panels shows the residuals, i.e. $(\text{measured energy} - \text{energy}) / \text{energy} \times 100\%$. The vertical dotted lines show the location of the Ga and As K-edges.

3.3 Energy resolution

The noise environment at the ESRF was worse than for HASYLAB, which is reflected in broader fwhm's. This can also be seen in the noise curves (Figure 4)

which show that the devices were dominated by parallel noise - most likely pickup on the FET input. For example, at the ESRF the 40 micron device showed an energy resolution of 880 eV at 10 keV slowly rising to ~ 1.25 keV at 35 keV. The corresponding resolution for the 400 micron device rises from 1.5 keV at 10 keV to ~ 1.6 keV at 35 keV and 1.8 keV at 175 keV. The noise environment at HASYLAB was more benign, with the shape of the noise curves more closely approximating the expected $t^{+0.5}$ and $t^{-0.5}$ dependencies for series and parallel noise. The 40 micron device had a fwhm energy resolution of ~ 700 eV at 10 keV rising slowly to 1.1 keV at 60 keV. The 400 micron device exhibited a similar dependence, with an energy resolution of 1.1 keV at 10 keV rising to 1.3 keV at 60 keV.

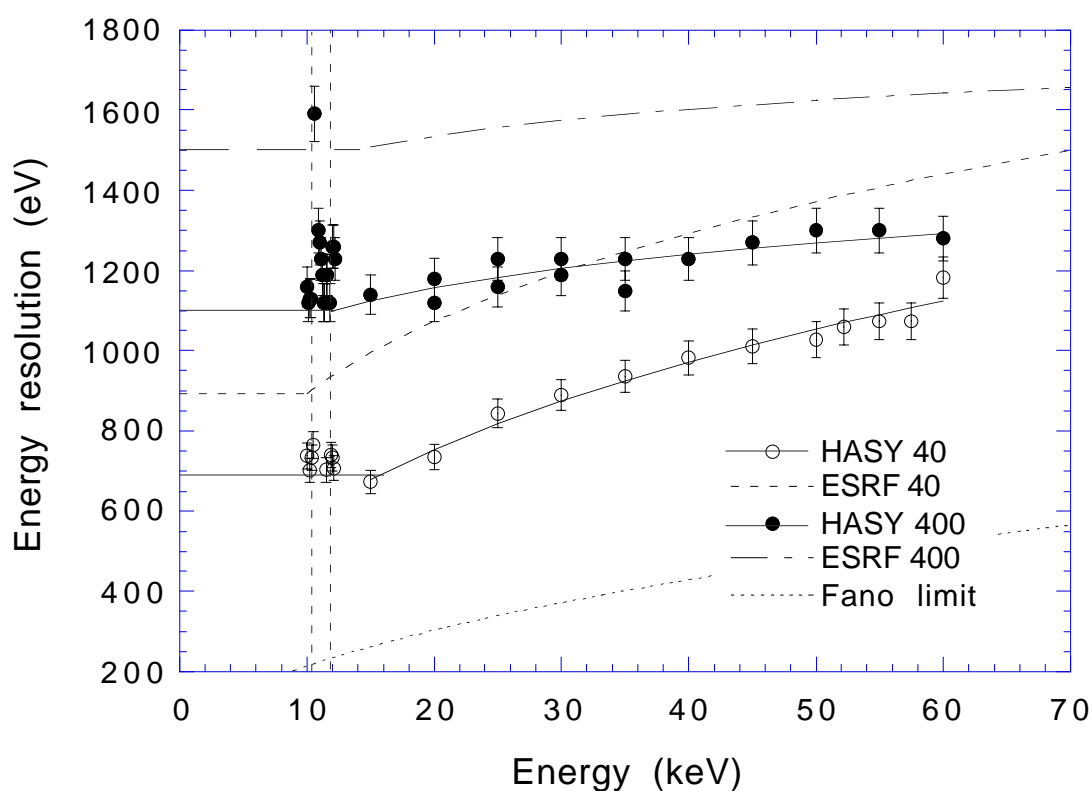


Figure 7. The energy dependent fwhm energy resolution of both devices measured at HASYLAB and the ESRF under pencil beam illumination. For clarity we only show the data points for HASYLAB, although the statistical uncertainties on the ESRF data are similar. The additional broadening around 10 keV is due to the Ga and As K-edges at 10.4 keV and 11.9 keV (shown by dotted lines) and is also seen in the ESRF data.

Figure 7 shows the energy dependent fwhm energy resolutions of both devices measured at HASYLAB and the ESRF under pencil beam ($20 \times 20 \mu\text{m}^2$) illumination. For comparison we also show the limiting energy resolution assuming a Fano factor of 0.18 [5]. For clarity we only show the HASYLAB data points and represent the ESRF data by best-fits. The statistical precision on both data sets is similar. The additional broadening around 10 keV is due to peak distortion by the Ga and As K-edges (shown

by the vertical dotted lines). All curves are well represented by simple powerlaws, varying as $\sim E^{0.3}$ for the 40 micron device and $\sim E^{0.1}$ for the 400 micron device. The horizontal extension of the dotted and solid lines below ~ 10 keV represents the electronic noise of the system, which for the 40 micron device was determined to be 690 eV fwhm at HASYLAB and 880 eV fwhm at the ESRF. For the 400 micron device, the corresponding figures were 1.5 keV fwhm at the ESRF and 1.1 keV fwhm

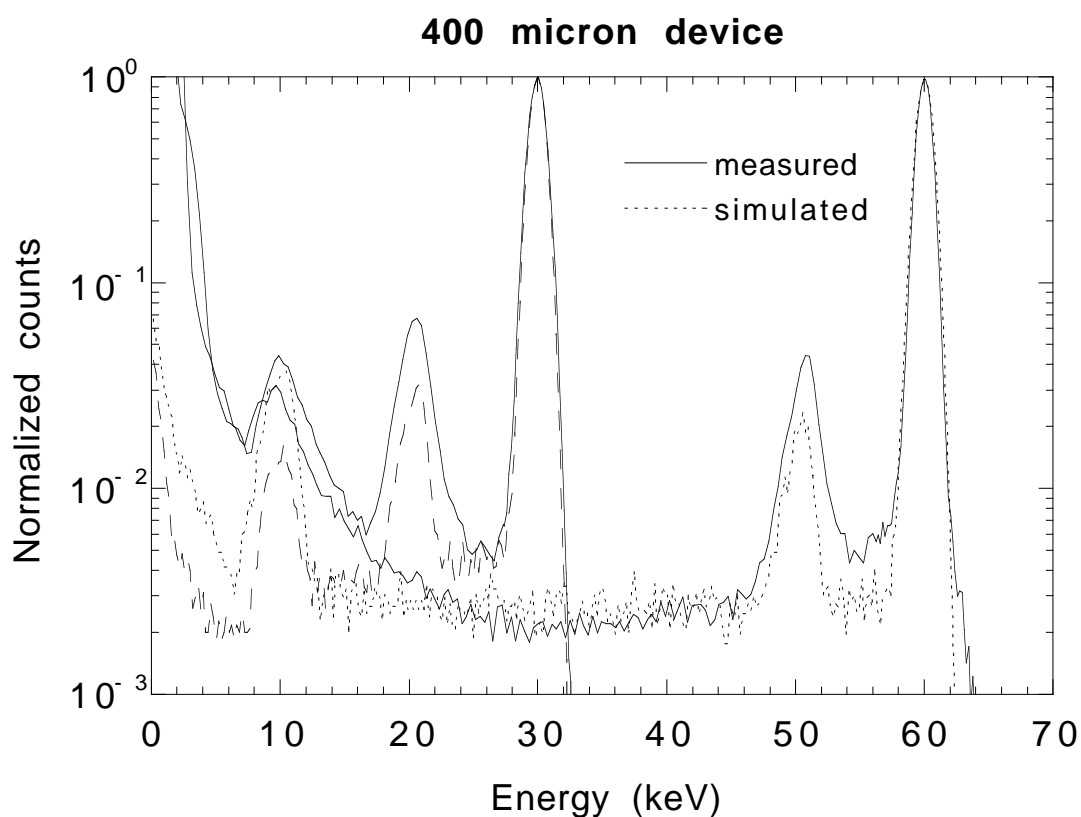


Figure 8. The energy loss spectra at 30 keV and 60 keV measured at HASYLAB. The dotted lines show the results of Monte-Carlo simulations.

at HASYLAB. The energy resolutions of both detectors were also measured under full area illumination at the ESRF using a Cd^{109} radioactive source. For the principal lines at 22, 25 and 88 keV, we find no statistically significant difference with those measured under pencil beam illumination.

3.4 Spectral response

In Figure 8, we show two detailed energy loss spectra measured by the 400 micron detector at HASYLAB. The incident beam energy was 30 keV and 60 keV. For comparison we also show the simulated spectrum based on the Monte-Carlo code described in Short [2]. The rise in continuum at low energies is due to a combination of charge loss resulting from field distortion at the detector edges and preferential

electron trapping in the low field region near the ohmic contact. The peak at ~ 10 keV is due to a combination of Ga and As fluorescent lines from the p+ layer. Likewise, the peaks located ~ 10 keV below the photopeaks are due to the Ga and As escape peaks. Note that while these peaks are unresolved in the 400 micron device, they are just resolved in the 40 micron device. We note from the Figure that the level of the continuum is extremely low, being only 1.0% on average of the photopeak at 30 keV falling to $\sim 0.2\%$ at 60 keV. The corresponding peak to total ratios are 84% and 95%, respectively, although most of the non-photopeak events are contained in lines. The large differences between the simulated and measured spectra at low energies is due to model limitations. Specifically, modeling the charge loss which results from a build up of space charge near the Schottky contact and non-uniformities in the electric field near the detector edges. By comparing the simulated and measured energy losses and then iteratively fine-tuning the model parameters, we find that the cross section-density products (σN) for electrons and holes are essentially zero indicating that the material used to fabricate these detectors is of excellent quality.

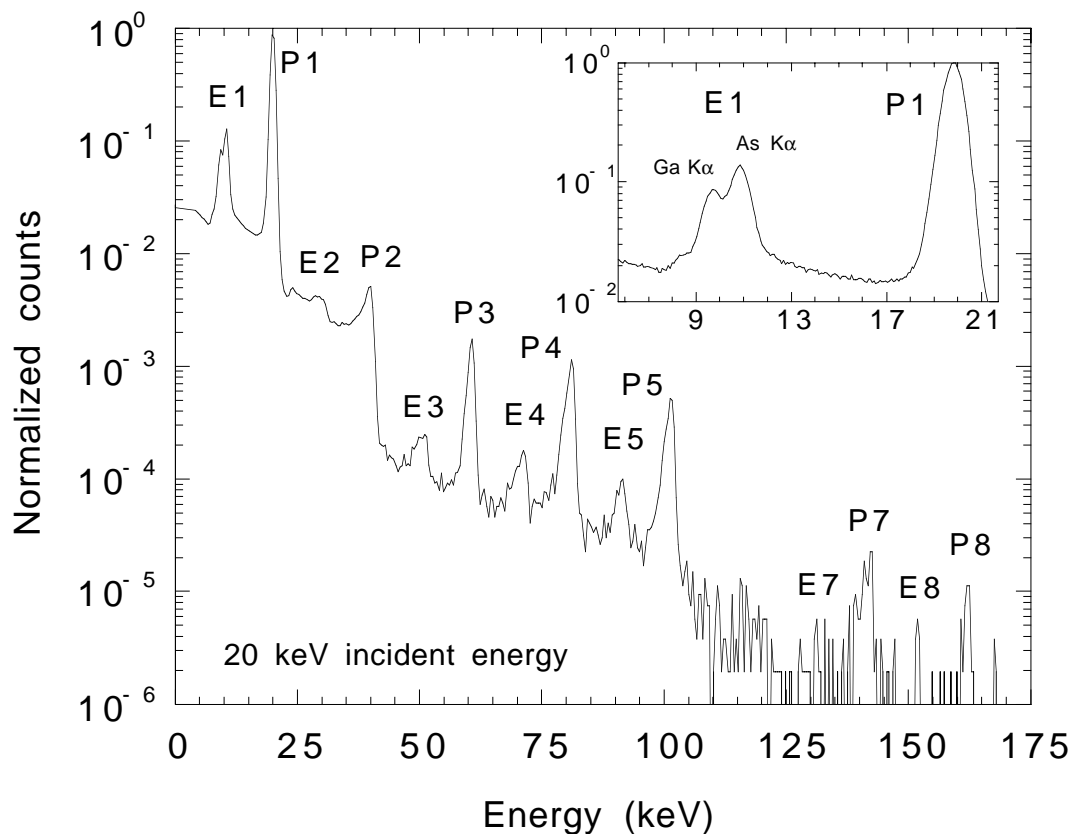


Figure 9. Energy spectrum measured at the ESRF with the 40 micron detector. Up to 5 harmonics (P3-P8) and their escape peaks (E3-E8) are clearly resolved. The insert shows in detail the energy-loss spectrum around the primary photopeak and its escape peaks.

Finally, in Figure 9 we show a 40 micron detector measurement of a 20 keV monochromatized synchrotron beam at the ESRF. Several mm of Al and Sn absorbers

have been inserted into the beam to enhance the higher orders. Here, P1 refers to the photopeak and P_n to the nth harmonic. E_n refers to the corresponding escape peaks. Up to 5 harmonics and their escape peaks are clearly resolved. Note, for Si[111] reflections, both the second and sixth harmonics are forbidden. The peaks designated, P2 and E2 are actually due to pile-up (i.e., two P1 or E1 events arriving within the resolving time of the electronics). The good energy resolution and sensitivity over such a wide dynamic range are clearly demonstrated, illustrating the diagnostic potential of GaAs detectors at synchrotron radiation (SR) facilities.

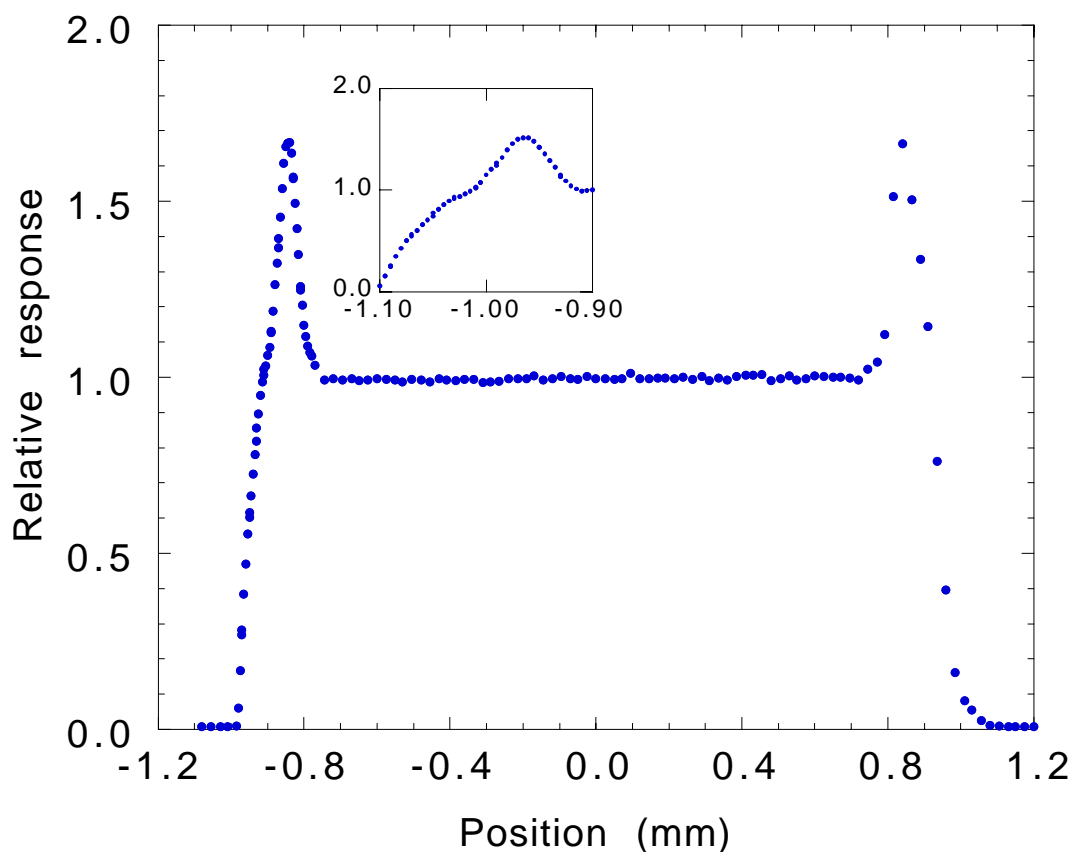


Figure 10. The variation in count rate across the 400 micron detector. The incident photon energy is 10 keV and the beam spot size $10 \times 10 \mu\text{m}^2$. The spatial resolution is $25 \mu\text{m}$. The inset shows a detailed scan of the left hand edge at $4 \mu\text{m}$ resolution.

3.5 Spatial uniformity

Using a series of slits, both before and after the monochromator, the incident beam could be adjusted down to a spot size of $10 \times 10 \mu\text{m}^2$ at the detector. The detectors were mounted on a 2-axis X-Y table capable of positioning each device to a precision of a few microns. Scans were carried out in X and Y across the detector to map its uniformity. For both the 40 and 400 micron detectors, the uniformity in response was in excess of 99% level. In Figure 10 we show a scan across the y-axis of the 400

device at an incident energy of 10 keV which corresponds to a penetration depth of ~ 50 microns. The spatial resolution is 25 microns. It is found that the response within the central 1 mm of the detector is constant within a percent and is consistent with both the statistical errors and the expected variation due to the non-uniformities in the thickness of the p+ layer ($\sim \pm 0.2 \mu\text{m}$). However, the response within ~ 0.2 mm of the edge begins to rise and is enhanced by $\sim 70\%$ at the edge. This is much greater than the error of individual measurements ($< 1\%$). The inset shows in detail the enhancement near the left hand edge at 4 microns resolution. Its rise and shape are due to transmission through the 1 mm wide etch ring in the dead layer separating the mesa and guard ring (see Figure 1), convolved with the beam size. The response then falls off linearly at the edge. This is consistent with the expected vignetting of the incident beam if the active region extends $\sim 100 \mu\text{m}$ beyond the mesa. The width of the distribution to the edge enhancements is 1.51 ± 0.03 mm which is the diameter of the mesa. However, we define the true active area to have a diameter equal to the fwhm of the distribution (excluding the edge peaks) which is 1.68 ± 0.03 mm - significantly larger than the physical diameter of the mesa. Surprisingly, this width was found to be independent of bias or energy. Results for the 40 micron device at 4 keV (penetration depth $4 \mu\text{m}$) have been presented elsewhere [1] and are essentially the same as those described above. A scan at 60 keV (penetration depth ~ 1 mm) is very similar to Figure 9 except that there are no longer enhancements near the edges. This demonstrates that the enhancements are indeed due to the etched ring between the mesa and guard-ring, since the p+ layer is transparent to X-rays of these energies. Assuming that additional charge loss mechanisms acting immediately at the detector boundary are negligible, we can deduce the thickness of the dead layer by the difference in transmission immediately before and after the mesa. For the 40 micron detector we calculate a thickness of $(6.1 \pm 0.3) \mu\text{m}$ and for the 400 micron detector $(25.4 \pm 0.1) \mu\text{m}$. Both values are very consistent with metrology.

4. Discussion and conclusions

These detectors yield some of the best performance figures yet reported for both full and pencil beam illumination [e.g. 3,4]. Although there is an order of magnitude difference in the thickness of the epi-layers of the two detectors, there is relatively little difference in energy resolutions. For example, at 10 keV the fwhm energy resolutions were 700 eV in the 40 micron detector and 1.2 keV in the 400 micron detector, at modest detector temperatures of -45 °C. At 60 keV, the corresponding resolutions were 1.0 and 1.3 keV. These should be compared to the calculated Fano resolutions [5] of ~ 220 eV and 525 eV at the same energies. At the lower energies, the measured resolution is dominated by leakage current and electromagnetic pick-up. However, at

medium and high energies, Fano noise becomes an appreciable fraction of the resolution function.

With the ability to produce 400 micron epitaxial layers we now have detectors with a sizeable efficiency extending into the hard X-ray band. This is illustrated in Figure 11, in which we show the calculated efficiencies of the two detectors across the energy range 1-1000 keV. For comparison, we also show the efficiency of a new 1 mm detector, which is at present being fabricated. Note, we have not included edge losses in this calculation, which will be severe at 1 MeV. This is because, eventually we intend to fabricate an array and the curve is solely to illustrate that such detectors offer the potential of bridging the gap between soft X- and gamma-ray energies.

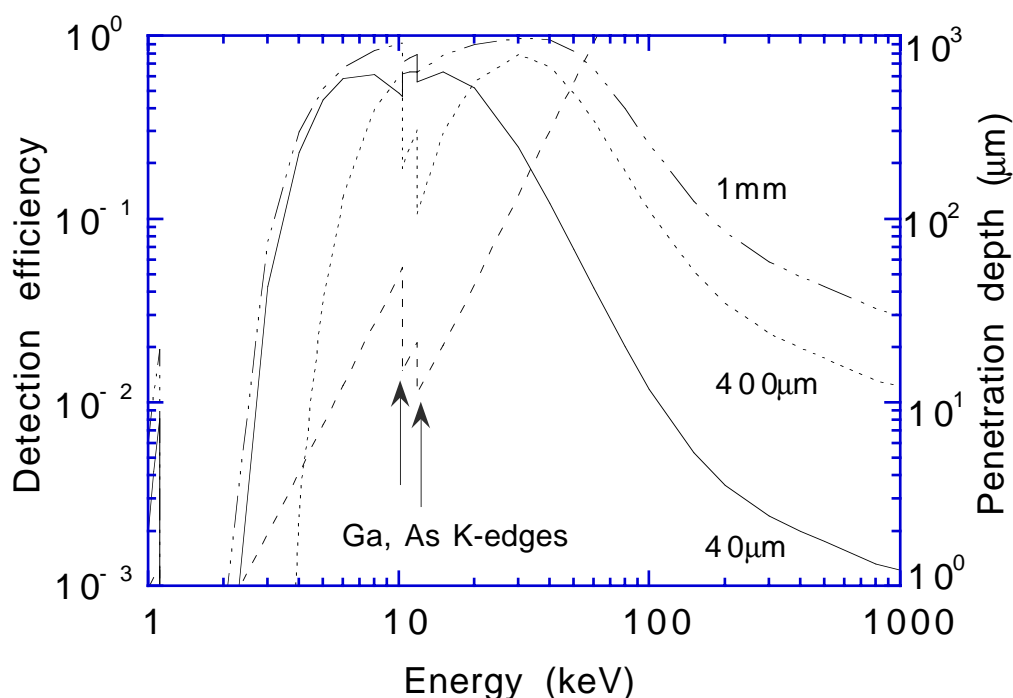


Figure 11. Calculated detection efficiencies of the 40 micron and 400 micron devices. The poor low energy response of the 400 micron device is due to its anomalous p+ layer thickness. For comparison, we also show the predicted efficiency of a new 1 mm thick epitaxial detector which is at present being fabricated.

Lastly, work is now being carried out to reduce pick-up noise, which is clearly a dominant component of the system noise. Measurements carried out in our laboratory show that potentially the 400 micron detector is capable of a limiting resolution 800 eV fwhm at 60 keV. This compares favorably with the Fano noise of 525 eV fwhm.

Acknowledgements

We thank J. Morse, A. Souvorov and L. Tröger for their contributions to this project. S. Kraft acknowledges an ESA Fellowship.

References

- [1] A. Owens, M. Bavdaz, S. Kraft, A. Peacock, H. Andersson, S. Nenonen, M. Gagliardi, T. Gagliardi, F. Scholtz and G. Ulm, *J. Appl. Phys.*, in press.
- [2] A. Short, PhD thesis, The University of Leicester (1997).
- [3] G. Bertuccio, A. Pullia, J. Lauter, A. Foster and H. Luth, *IEEE Trans. Nucl. Sci.* **44**, 1 (1997).
- [4] T.J. Sumner, S.M. Grant, D. Alexiev and K.S.A. Butcher, *Nucl. Instr. and Meth.* **A348**, 518 (1994).
- [5] J.E. Eberhardt, R.D. Ryan and A.J. Tavendale, *Nucl. Instr. and Meth.*, **94**, 463 (1971).